Electronic Supplementary Material (ESI) for ChemComm.

Supplementary Information for

New insights into aging in $LiNiO_2$ cathodes from high resolution paramagnetic NMR spectroscopy

Nguyen, H.,[1,2] Kurzhals, P.,[3] Bianchini, M.,[3,4,] Seidel, K.,[3] and Clément, R. J.[1,2]*

[1]Materials Department, University of California, Santa Barbara, CA 93106, USA
[2]Materials Research Laboratory, University of California, Santa Barbara, CA 93106, USA
[3]BASF SE, Ludwigshafen am Rhein, 67056, Germany
[4]University of Bayreuth, Bavarian Center for Battery Technology (BayBatt), Bayreuth, 95447, Germany

* Email: rclement@ucsb.edu

Experimental details

Material Synthesis: $Li_{1-y}Ni_{1+y}O_2$ active materials were synthesized using a solid-state synthesis route from coprecipitated $Ni(OH)_2$ precursors (Hunan Zoomwe Zhengyuan Advanced Material Trade Co., Ltd). $LiOH{\cdot}H_2O$ (Albemarle Corporation) was ground prior to the synthesis and mixed with $Ni(OH)_2$ in a laboratory blender (Kinematica AG). Li:Ni mol ratio of 1.04 was used. The mixture was placed in a ceramic crucible (Al_2O_3) and fired in a laboratory box-type furnace (inn High Therm GmbH) under a flowing pure O_2 environment. The mixture was first heated to 400 °C and fixed at that temperature for 4 h and then the temperature was ramped up to 700 °C and held there for 6 h. A ramp rate of 3 °C was used for both heating steps.

Electrochemistry: Free-standing LNO: carbon black (Super C65; MTI Corporation): polytetrafluoroethylene (PTFE; Sigma Aldrich) films were fabricated in a mass ratio of 94:3:3. The electrode was cycled in Li half cells using Swagelok cells, 1 M LiPF6 in ethylene carbonate, dimethylcarbonate, and diethylcarbonate (EC/DMC/DEC = 1/1/1 v/v/v) electrolyte, and Whatman GF/D glass microfiber separators. Cells were cycled from 3.0 V to an upper voltage cutoff of either 4.1 V or 4.3 V vs. Li/Li^+ at a rate of C/10 (1 C = 200 mA g^{-1}). The loading density for the electrodes were ≈11-15 mg cm^{-2}. All cells were cycled on an Arbin BT2000 or Bio-logic VMP-3e potentiostat. *Ex situ* samples were prepared by cycling to the desired conditions and extracting the cathode inside an Ar filled glovebox. *Ex situ* samples were washed in DMC (Sigma) and dried under vacuum before analysis.

X-ray Diffraction: Ex situ samples were loaded into glass capillaries to prevent air exposure and measured at Beamline 11-BM at the Advanced Photon Source (APS). A Kapton sleeve was used to mount the samples. All patterns were collected in Debye–Scherrer geometry from 0.5° to 50° 2θ at room temperature with data points collected every 0.001° 2θ and a scan speed of 0.01°/s. The broad resonance at low angles in the patterns results from the amorphous glass capillary and Kapton. Refinements were conducted using the TOPAS software suite[1] and detailed in **ESI Note 2.**

Magnetometry: Samples were loaded into sealed quartz tubes (1 mm ID and 3 mm OD). SiO_2 powder (Advalue Tech) was used to center the cathode samples inside the quartz tubes. Measurements were done on a Quantum Design MPMS3 SQUID magnetometer. Zero field and field cooled M(T) measurements were carried out from 2 to 350 K with H = 0.1 T.

NMR: Solid state ^7Li NMR measurements were done on a wide bore Bruker BioSpin spectrometer with a DMX 500 MHz console and a home built 1.3 single X-broadband magic angle spinning (MAS) probe. All spectra were acquired at B_0 = 2.35 T (100 MHz for ^1H) with 60 kHz MAS using dry nitrogen and the probe was tuned to ^7Li (38.9 MHz). Samples were packed into 1.3 mm zirconia rotors inside an Ar glovebox and closed with Vespel caps. ^7Li chemical shifts were referenced to 0 ppm with 1M aqueous LiCl solutions. All acquisitions were done with a rotor synchronized spin-echo sequence with a 90° pulse of 0.45 μs. A recycle delay of 50 ms was sufficient for paramagnetic signals to be fully relaxed. NMR data was processed using Bruker TopSpin 3.6.5 and spectral fits were done with DMfit.[2] An initial fit on T2 filtered spectra was performed to determine spectral parameters of slow relaxing environments. These values were then fixed in a subsequent fit on spectra acquired with a 0.45 μs pulse. Mixed Gaussian-Lorentzian lineshapes were used and the minimum number of resonances were used.

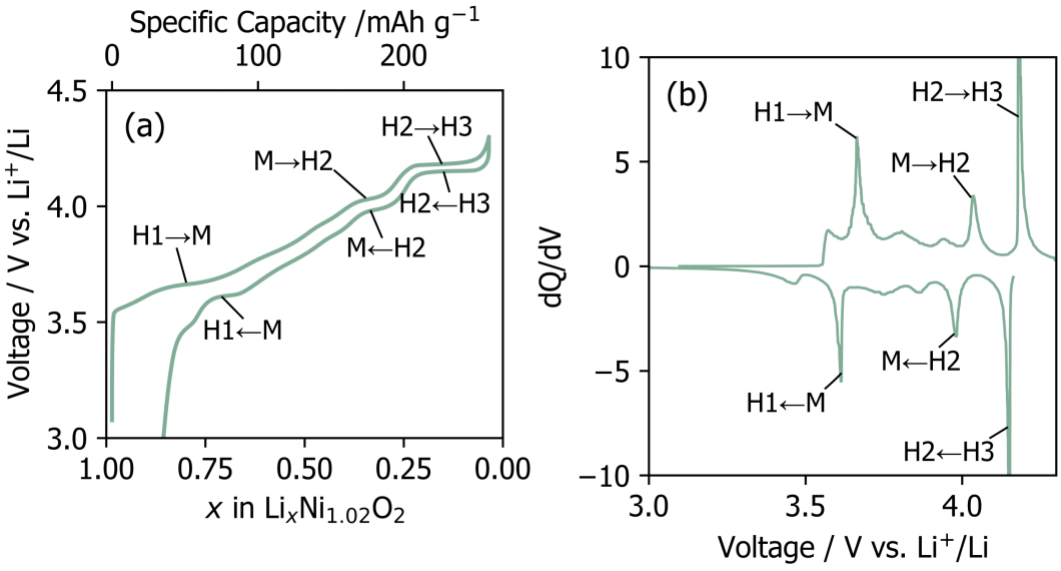

Fig. S1 (a) Voltage profile and (b) differential capacity (dQ/dV in mAh g^{-1} V^{-1}) curve obtained during the first charge-discharge cycle, with phase transitions indicated.

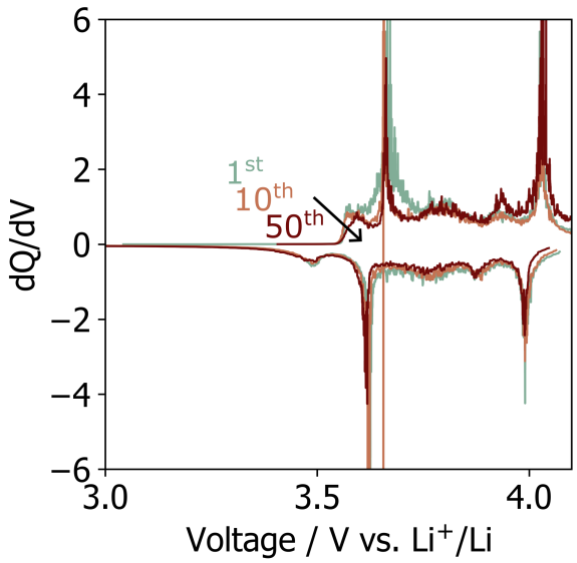

Fig. S2 Differential capacity (dQ/dV in mAh g^{-1} V^{-1}) curves obtained during the 1st, 10th, and 50th cycle of LNO when using a 4.1V upper voltage cutoff.

ESI Note 1. Analysis of the differential capacity curves obtained for LNO half- cells cycled up to 4.1 or 4.3 V vs. Li/Li^+

Differential capacity (dQ/dV) analysis was carried out to better understand the changes in the electrochemical processes taking place upon extended operation. Differential capacity plots for the 1st and 10th cycles for cells cycled up to 4.3 V (**Fig. 1c**) exhibit three prominent dQ/dV peaks that correspond to the two-phase reactions associated with the H1 to M, M to H2, and H3 to H3 phase transitions[3,4], while the 50th cycle differential capacity plot is relatively featureless. Local minima between H1 to M and M to H2 phase transitions in the differential capacity plot for the 1st cycle have been attributed to stable Li-vacancy orderings in the bulk at those compositions.[4,5] Interestingly, the minimum immediately after the H1→M transition is no longer present at the 10th cycle, which cannot simply be explained by an increase in impedance since this would lead to a shift of all of the peaks. The loss of the dQ/dV minimum suggests instead that the Li-vacancy orderings are disrupted by the structural changes taking place during cycling. In contrast, the dQ/dV features observed for cells cycled up to 4.1 V (**Fig. S2)** are relatively stable, with peak and local minima positions not changing significantly during extended cycling. The most notable change for the 4.1 V cells is the narrowing of the dQ/dV peak associated with the H1 to M phase transition on charge.

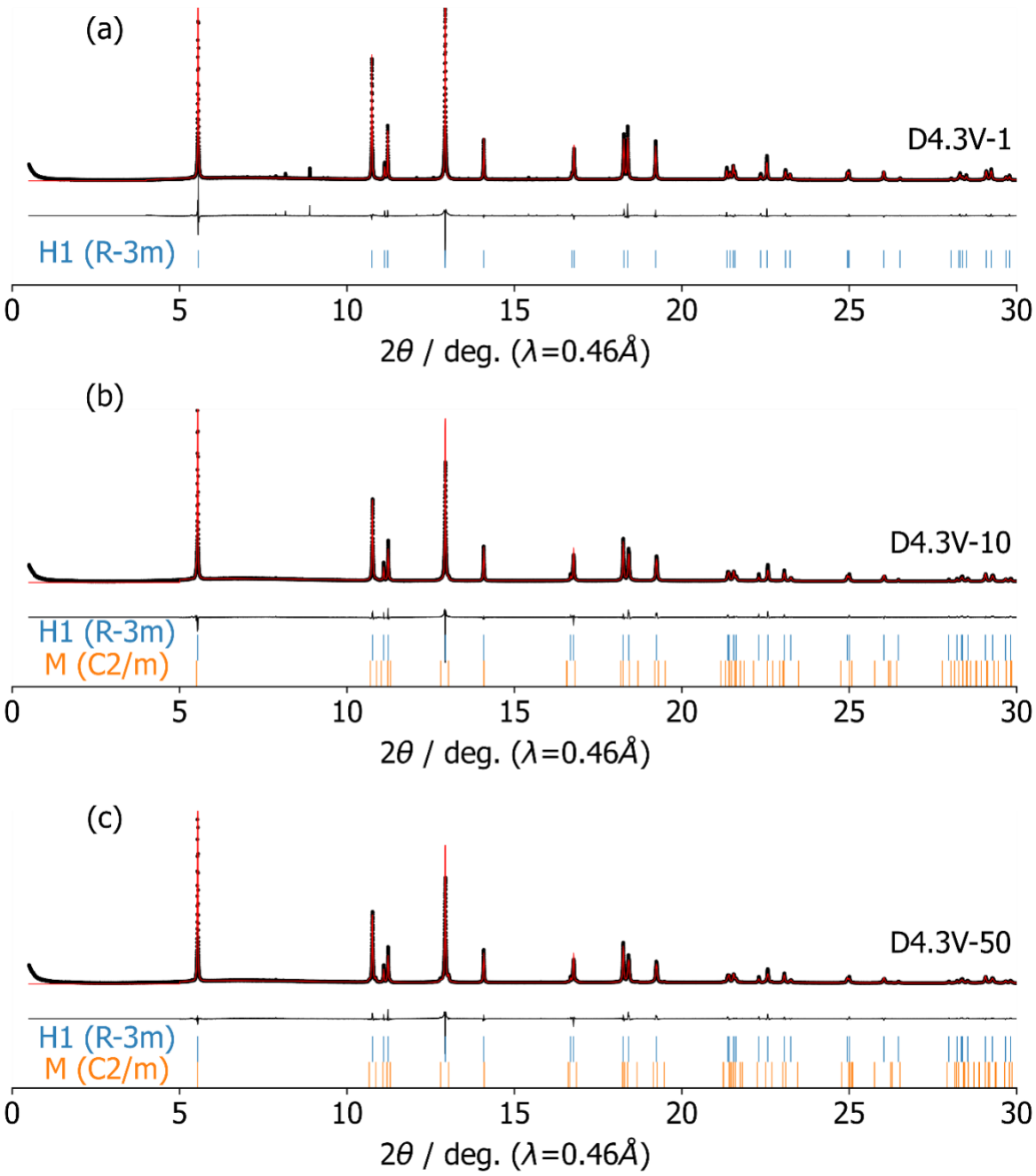

Fig. S3 Full synchrotron XRD patterns collected on the D4.3V sample series: (a) D4.3V-1 (b) D4.3V-10 (c) D4.3V-50.

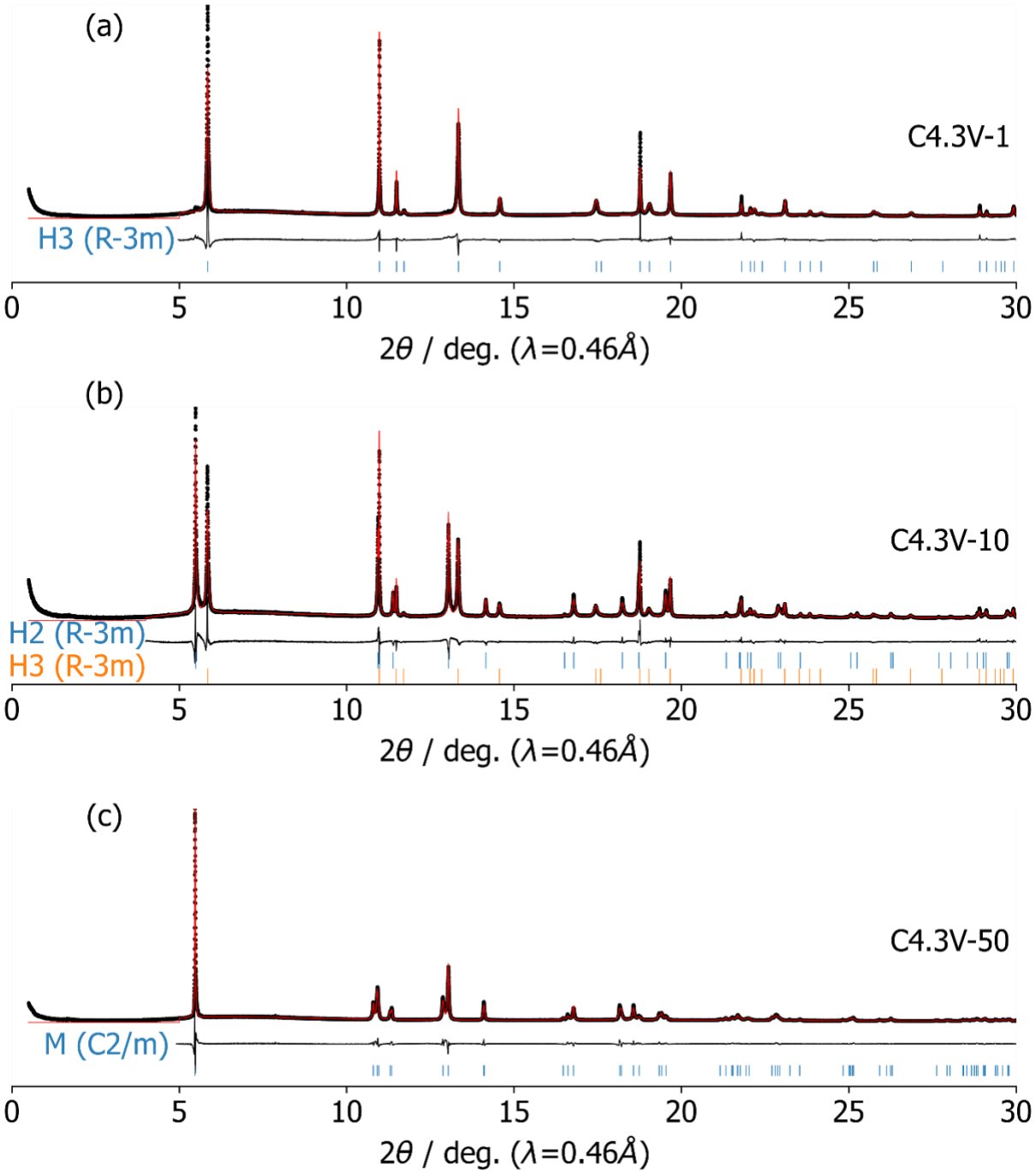

Fig. S4 Full synchrotron XRD patterns collected on the C4.3V sample series: (a) C4.3V-1 (b) C4.3V-10 (c) C4.3V-50.

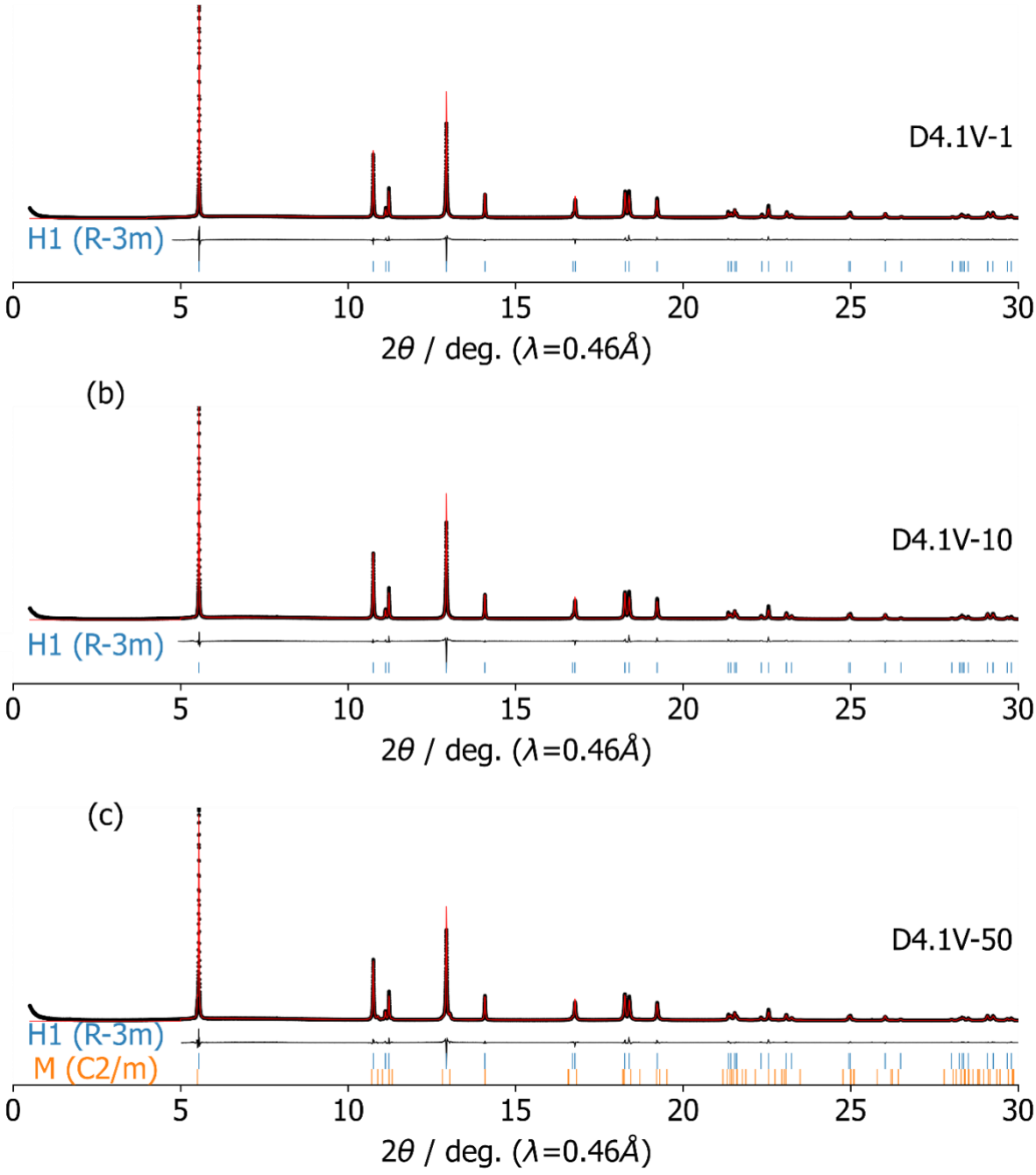

Fig. S5 Full synchrotron XRD patterns collected on the D4.1V sample series: (a) D4.1V-1 (b) D4.1V-10 (c) D4.1V-50.

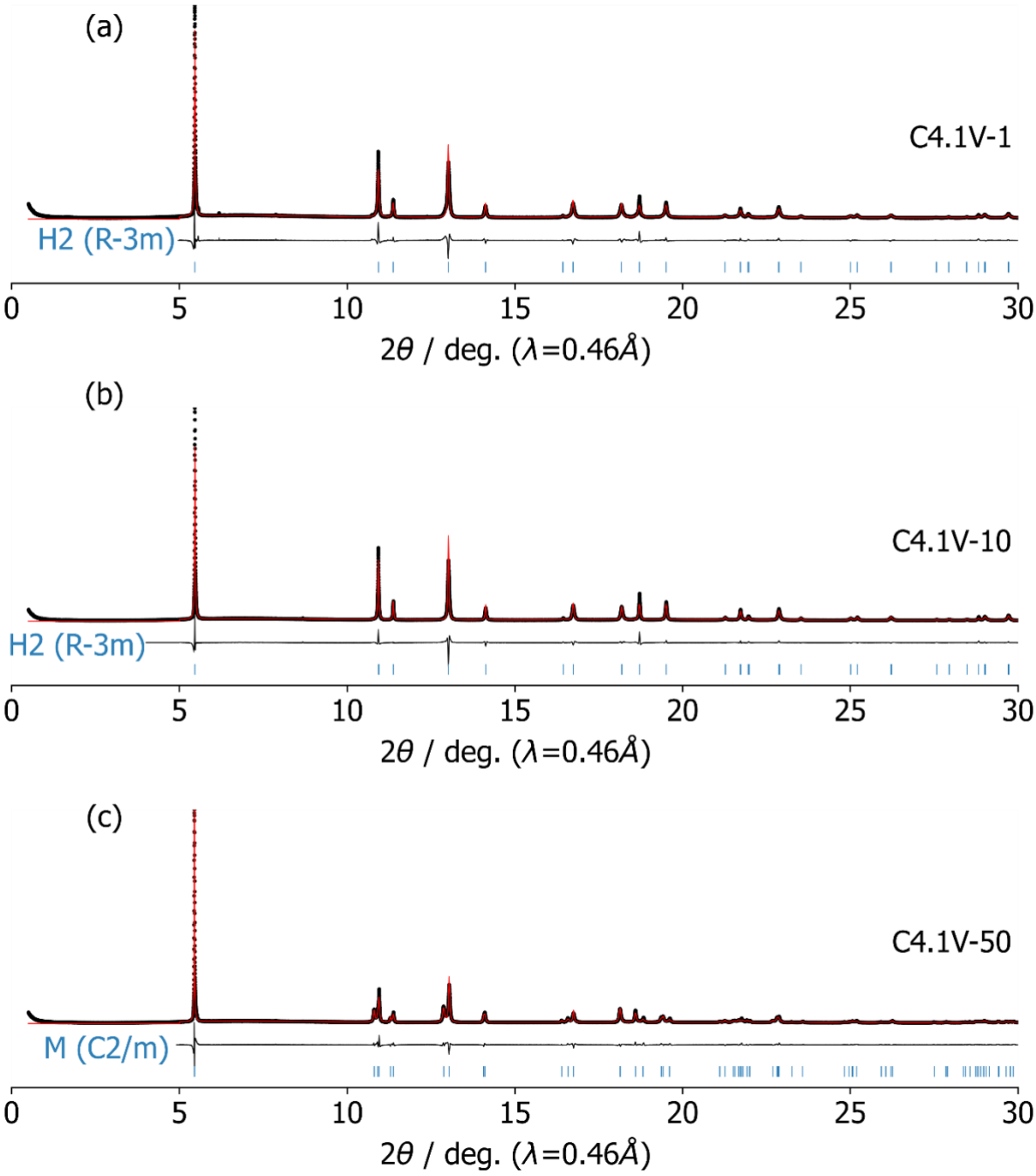

Fig. S6 Full synchrotron XRD patterns collected on the C4.1V sample series: (a) C4.1V-1 (b) C4.1V-10 (c) C4.1V-50.

Table S1. Structural refinement parameters for synchrotron XRD data presented in this work.

Sample	Rwp	Phase 1									Phase2								
		Space Group	a (Å)	B (Å)	c (Å)	be (°)	O_x	O_z	Ni_Li	Phase fraction	Space Group	a (Å)	B (Å)	c (Å)	be (°)	O_x	O_z	Ni_Li	Phase Fraction
C4.3V-1	12.2	R-3m	2.8152 (4)	-	13.4978 (2)	-	-	0.2638 (1)	0.0151 (7)	1									
C4.3V-10	10.3	R-3m	2.8165 (3)	-	13.5120 (2)	-	-	0.2649 (1)	0.0173 (8)	0.52	R-3m	2.8215 (4)	-	14.3855 (2)	-	-	0.264 (1)	0.0169 (8)	0.48
C4.3V-50	9.1	C2/m	4.9438 (6)	2.8195 (4)	5.0950 (8)	109.3484 (7)	0.2638 (3)	0.7868 (2)	0.0317 (7)	1									
D4.3V-1	10.0	R-3m	2.8741 (1)	-	14.2127 (6)	-	-	0.2593 (1)	0.0151 (4)	1									
D4.3V-10	9.4	R-3m	2.8693 (1)	-	14.2462 (7)	-	-	0.2597 (1)	0.0151 (4)	0.94	C2/m	4.9896 (8)	2.8279 (3)	5.0805 (5)	109.784 (1)	0.256 (4)	0.784 (3)	0.015*	0.06
D4.3V-50	9.2	R-3m	2.8698 (1)	-	14.2456 (7)	-	-	0.2597 (1)	0.0150 (4)	0.9	C2/m	5.0040 (2)	2.8322 (1)	5.0597 (3)	109.905 (4)	0.278 (2)	0.796 (2)	0.015*	0.1
C4.1V-1	10.6	R-3m	2.8235 (6)	-	14.4522 (3)	-	-	0.2650 (1)	0.0160 (7)	1									
C4.1V-10	11.6	R-3m	2.8231 (4)	-	14.4443 (2)	-	-	0.2651 (1)	0.0153 (6)	1									
C4.1V-50	10.6	C2/m	4.9403 (7)	2.8074 (5)	5.1112 (7)	109.1596 (7)	0.2648 (3)	0.7899 (2)	0.0173 (6)	1									
D4.1V-1	8.7	R-3m	2.8734 (1)	-	14.2153 (7)	-	-	0.2593 (4)	0.0156 (4)	1									
D4.1V-10	8.8	R-3m	2.8724 (1)	-	14.2228 (7)	-	-	0.2594 (5)	0.0175 (4)	1									
D4.1V-50	8.2	R-3m	2.8722 (1)	-	14.2275 (7)	-	-	0.2602 (1)	0.0150 (4)	0.89	C2/m	4.9882 (3)	2.8240 (1)	5.0770 (2)	109.718 (4)	0.223 (1)	0.754 (1)	0.015*	0.11

* Ni_Li occupancy was fixed to 0.015 for M phases in D4.3V-10, D4.3V-50, and D4.1V-50

ESI Note 2. Inferring the broad evolution of the Li content of LNO fatigued domains from their lattice parameters

Protocol for the analysis of the synchrotron XRD data: A Le Bail fit of the synchrotron XRD data collected on the various *ex situ* samples of interest was performed to identify the crystalline phase(s) present in each sample, and determine their space group and refined lattice parameters. The background was fit with a Chebyshev polynomial (10 terms) and additional refinement parameters included axial divergence, crystallite size, microstrain, zero shift, and absorption. These values were fixed in a following Rietveld refinement to obtain the occupancy of Li (3a) sites by Ni (Ni_{Li} occupancy). In the Rietveld refinement, Debye-Waller factors were fixed based on published values of $Li_{0.98}Ni_{1.02}O_2$ (ICSD collection code 14676): 0.8 for oxygen, 0.6 for atoms in 3a sites, and 0.3 for atoms in 3b sites. The total Ni content was fixed to 1.015 and the Ni occupancy factors of the 3a and 3b cation sites of the *R*-3*m* structure were allowed to vary. Stephens peak shapes were used to model anisotropic broadening effects in samples obtained from cycled cells.[6] An attempt to refine for Ni migration into tetrahedral sites on charge led to an unrealistically large fraction of migrated Ni (~0.15) on first charge (C4.3V-1 sample), which remains stable after 10 cycles (C4.3V-10 sample). These results are inconsistent with the NMR and magnetometry results obtained on the same samples and are disregarded hereafter.

While a direct relationship has been established between LNO lattice parameters and the Li content in the layered structure during the first charge-discharge cycle[3,4], differences in Ni off-stoichiometry between as-prepared $Li_{1-y}Ni_{1+y}O_2$ samples, and structural degradation during cycling complicate the analysis. Hence, we use a pragmatic approach and instead compare the lattice parameters of similar (e.g., hexagonal (H), or monoclinic (M)) phases present across *ex situ* samples of a given series to infer the general evolution of their Li content as a function cycling.

Analysis of discharged samples: All discharged samples are comprised of a major H1 phase (synchrotron XRD patterns for the D4.1V and D4.3V samples are shown in **Figures 2a** and **2c**, respectively), but additional reflections that belong to a monoclinic (M) phase are present in the patterns collected on the D4.3V-10, D4.3V-50, and D4.1V-50 samples. The $(003)_{H1}$ reflection shifts to lower angles from D4.3V-1 to D4.3V-10, corresponding to an increase in the *c* lattice parameter from 14.2127(6) Å to 14.2462(7) Å and to a decrease in the Li content within the H1 phase after 10 cycles. A similar $(003)_{H1}$ position and *c* lattice parameter is observed for the D4.3V-10 and D4.3V-50 samples, and hence very little change in Li content between these two phases. When it comes to the M phase, the $(001)_M$ reflection overlaps with the $(003)_{H1}$ peak and we therefore focus on the $(20\bar{2})_M$ and $(111)_M$ peak positions hereafter. The positions of the $(20\bar{2})_M$ and the $(111)_M$ reflections for D4.3V-10 and D4.3V-50 are similar, which suggests that the M phases in these two samples have similar Li contents. Clearly, the aged cathode still partially converts from the

intermediate M phase to the final H1 phase on discharge, as indicated by the smaller M phase fraction in D4.3V-10 (6 wt%) as compared to D4.3V-50 (10 wt%), consistent with a gradual loss of Li inventory.

The loss of Li inventory occurs at a slower rate when LNO is charged up to 4.1V, since the M phase can only be observed in the 50th cycle discharged sample (D4.1V-50). The $(003)_{H1}$ peak shifts to lower angles across the D4.1V sample series, corresponding to an increase in *c* lattice parameter from 14.2153(7) Å (D4.1V-1), to 14.2228(7) Å (D4.1V-10), to 14.2275(7) Å (D4.1V-50) and a decrease in Li content. While the *c* lattice parameters of the H1 phases present in the D4.1V and D4.3V samples are similar at cycle 1, the H1 phases present in the D4.1V-10 and D4.1V-50 samples contain more Li than those present in the D4.3V-10 and D4.3V-50 samples. The $(20\bar{2})_M$ and the $(111)_M$ peak for D4.1V-50 have the same positions as the D4.3V-10 and D4.3V-50 samples.

Analysis of charged samples: While the XRD patterns collected on cathode samples in the discharged state are overall quite similar, there are substantial differences between patterns obtained on samples stopped at 4.1 V (**Fig 2b**) or 4.3 V (**Fig 2d**) on charge. In the absence of structural degradation, the C4.1V samples should be entirely H2, and the C4.3V samples should be entirely H3. A single H2 phase is indeed observed for C4.1V-1 and C4.1V-10, with a small difference in *c* lattice parameter between the two samples (14.45 Å and 14.44 Å, respectively). In the H2 phase region, a decrease in *c* lattice parameter is observed with decreasing Li content, which allows us to infer that the H2 phase in C4.1V-10 has a slightly lower Li content than that in C4.1V-1. In contrast, C4.1V-50 exhibits a single M phase, consistent with gradual structural degradation resulting in less effective Li extraction from the LNO cathode after 50 cycles. C4.3V samples are notoriously hard to fit due to anisotropic broadening and stacking faults that lead to high residuals.[4,7] While the C4.3V-1 sample contains a single H3 phase with a very low Li content (0.01 based on charge passed), as expected, the C4.3V-10 sample contains a mixture of H2 and H3 phases, and the C4.3V-50 sample exhibits a single M phase, again suggesting a gradual loss of electrochemical activity that is more pronounced as the cathode is cycled above 4.1 V due to anisotropic lattice changes that lead to particle cracking and a rise in surface impedance. Overall, the *ex situ* synchrotron XRD analysis reveals that aging of LNO mostly hinders Li extraction at high states of charge, with the M-H2 and H2-H3 phase transitions becoming inaccessible after 50 cycles, irrespective of the upper cutoff voltage, while Li-rich compositions (within the H1 compositional range) can be accessed in the discharged state. This loss of accessible capacity during the high voltage charge processes is similarly observed in Ni-rich NMCs.[8–11]

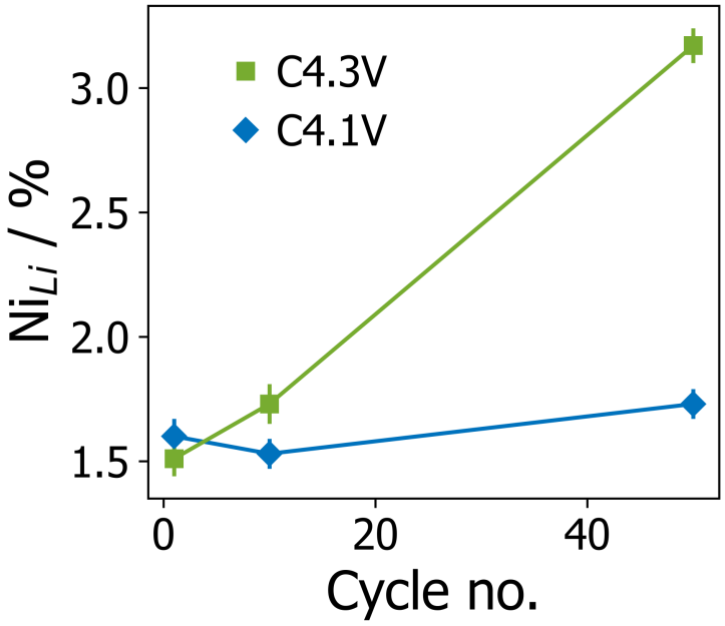

Fig. S7 Ni migration determined by Rietveld refinements of synchrotron XRD data collected on charged samples. A molar weighted average value is plotted for sample C4.3V-10 due to multiple phases.

Table S2. Magnetic moments and Curie-Weiss constants derived from Curie-Weiss fits of the magnetic susceptibility data. Data was fit to the equation: $\chi = \frac{C}{T-\theta_{cw}} + \chi_0$, where $\mu_{eff} = \sqrt{8C}$.

Sample	**μ_{eff} (μ_B)**	**θ_{cw} (K)**	**χ_0**
As-synthesized $Li_{0.98}Ni_{1.02}O_2$*	1.83(1)	36(1)	-
Pristine electrode	2.20(1)	41(1)	2.39E-04
D4.3V-1	2.07(6)	27(7)	5.07E-05
D4.3V-10	2.02(4)	47(4)	1.72E-04
D4.3V-50	1.90(4)	65(5)	2.04E-04
C4.3V-1	0.38(4)	91(17)	1.42E-04
C4.3V-10	0.99(2)	33(4)	2.48E-05
C4.3V-50	1.37(9)	52(13)	1.76E-04
D4.1V-1	2.05(5)	33(6)	7.77E-05
D4.1V-10	1.91(1)	53(2)	3.18E-04
D4.1V-50	1.67(5)	88(5)	4.93E-04
C4.1V-1	1.19(4)	35(8)	2.96E-04
C4.1V-10	1.00(3)	40(6)	3.18E-04
C4.1V-50	0.98(1)	35(3)	2.15E-04

* these results are reproduced from prior work.[12]

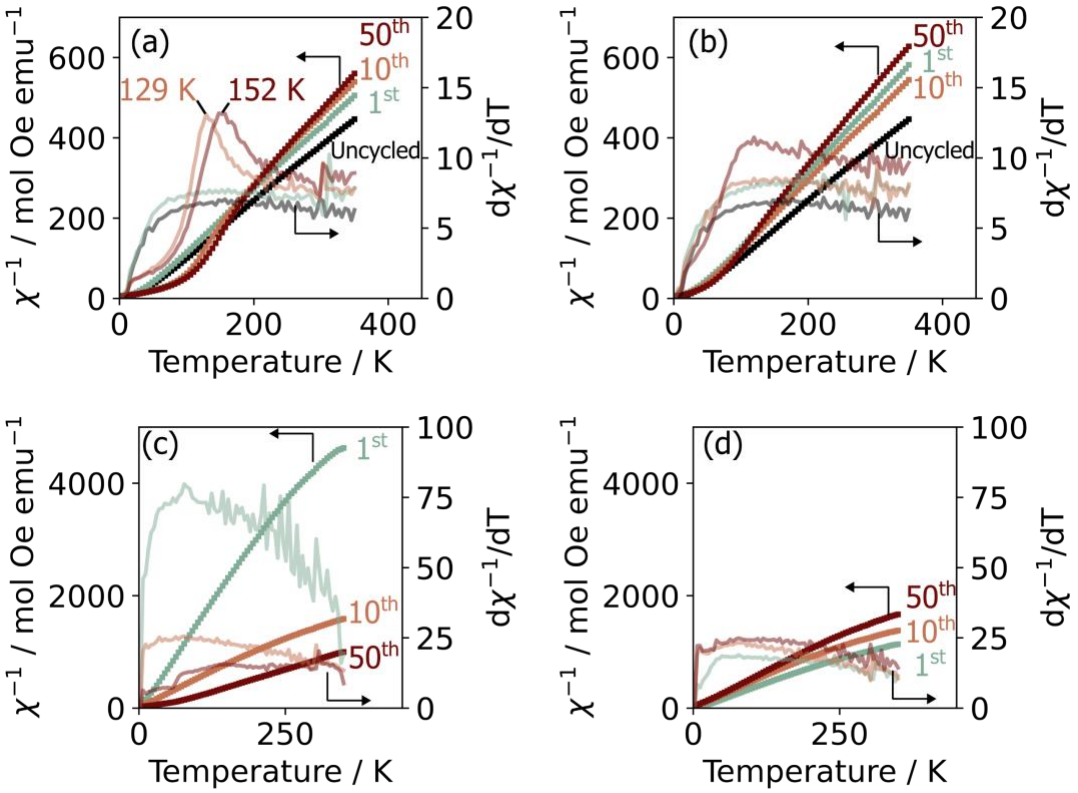

Fig. S8 Inverse magnetic susceptibility (χ^{-1}) vs. temperature (T) curves collected on *ex situ* samples after the 1st, 10th and 50th cycle for (a) D4.3V, (b) D4.1V, (c) C4.3V, and (d) C4.1V. Magnetic transition temperatures are identified by the differential magnetic susceptibility, $d\chi^{-1}/dT$ (mol Oe emu^{-1} T^{-1}), shown in the secondary y-axis.

ESI Note 3. Evolution of the magnetic properties with cycling

The inverse magnetic susceptibility (χ^{-1}) vs. temperature data curves (and derivative ($d\chi^{-1}/dT$) curves) obtained for the discharged (D4.3V and D4.1V) sample series are shown in **Fig. S8**. The effective magnetic moments (μ_{eff}) and Curie-Weiss constants (θ_{cw}) obtained from fits of the magnetic susceptibility data in the paramagnetic (Curie-Weiss) regime are listed in **Table S2**. Curie-Weiss parameters, μ_{eff} and θ_{cw}, for as-synthesized LNO is consistent with prior work.[13] The effective magnetic moments of the D4.3V-1 and D4.1V-1 samples, of 2.07(6) μ_B and 2.05(5) μ_B, respectively, are higher than the spin-only (so) magnetic moment computed assuming a stoichiometric $LiNiO_2$ composition (μ_{so} = 1.73 μ_B). The larger magnetic moments obtained for the cycled cathode samples are likely due to processing the material into electrodes with carbon additives and/or binder as observed in the larger μ_{eff} of the uncycled LNO electrode (2.20(1) μ_B) when compared to that of the as-synthesized material (1.83 μ_B, reported in our prior work[12]). Despite this additional magnetic contribution, the trends in μ_{eff} and θ_{cw} with cycle number provide insight into the degradation modes in LNO assuming that the contribution from non-LNO components does not change with aging. The effective magnetic moment obtained for *ex situ* samples in the discharged state shows a general decreasing trend from cycle 1 to 50, evolving from 2.07(6) μ_B to 1.90(4) μ_B for the D4.3V samples, and from 2.05(5) μ_B to 1.67(5) μ_B for the D4.1V samples. The main cause of the decreasing magnetic moment is likely the presence of residual Ni^{4+} on discharge, due to incomplete utilization of the $Ni^{3+/4+}$ redox reservoir in aged cathodes, as discussed in the main text. Interestingly, the decrease in the effective magnetic moment with cycling is not as pronounced for the D4.3V samples as for the D4.1V samples, which could suggest at first glance that the structure of the cathode is more reversible when cycled over the larger voltage range, in contradiction with the synchrotron XRD results presented earlier. Another possibility is that the larger effective magnetic moments measured for the aged 4.3V samples result from a larger fraction of Ni^{2+}, which would be consistent with Ni migration into the interlayer space.

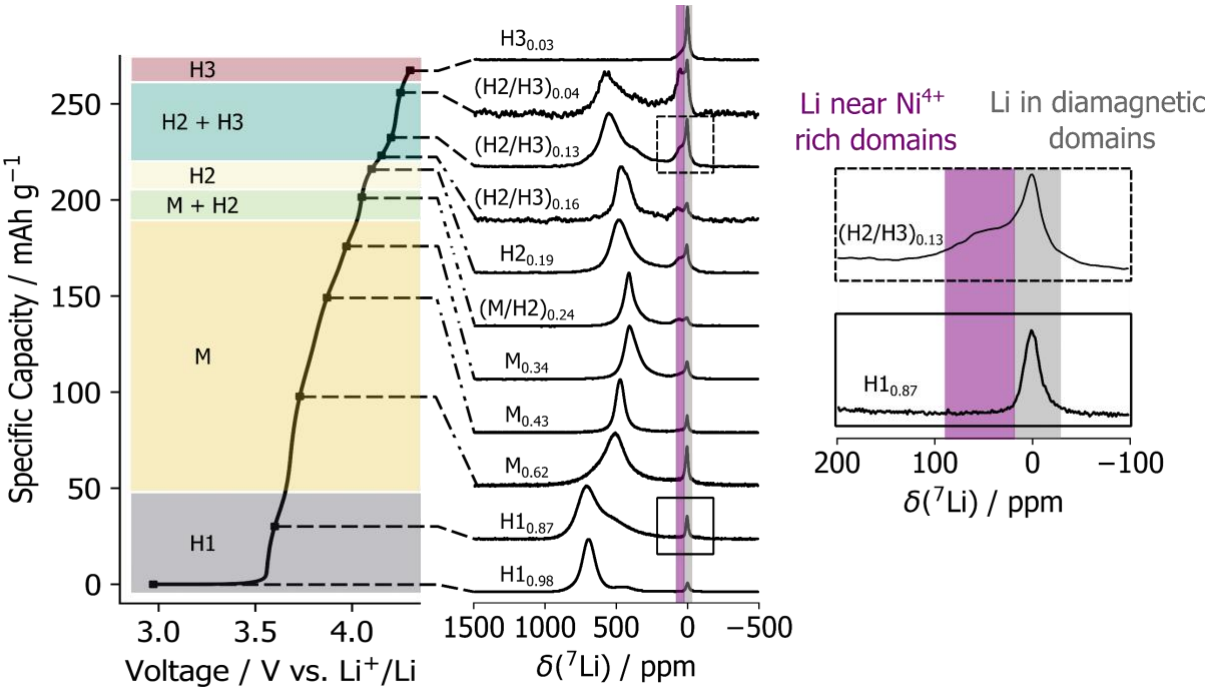

Fig. S9 ^{7}Li solid-state NMR spectra collected on *ex situ* cathode samples obtained at various stages during the first charge process. The sample labeling scheme adopted here comprises the symmetry label of the LNO phase(s) present in the sample at a given state of charge and the nominal Li content derived from the specific capacity. The spectral evolution during the first charge process is consistent with previously reported spectra.[14] The NMR parameters obtained from fits of the spectra are summarized in **Table S3** below.

Table S3. Summary of ^{7}Li NMR parameters obtained from fits of the NMR spectra obtained on *ex situ* LNO samples during the first charge process, along with other key descriptors of these samples.

V vs. Li/Li+	*x* in $Li_xNi_{1.02}O_2$	sXRD phase(s)	Resonance 1				Resonance 2				Resonance 3				Resonance 4			
			δ / ppm	Intensity (a.u.)*	Line width (hz)	T2 (ms)	δ / ppm	Intensity (a.u.)*	Line width (hz)	T2 (ms)	δ / ppm	Intensity (a.u.)*	Line width (hz)	T2 (ms)	δ / ppm	Intensity (a.u.)*	Line width (hz)	T2 (ms)
OCV	0.98	H1	695	0.908	4262	2.390	448	0.092	5862	3.810								
3.60	0.87	H1	715	0.361	5480	0.505	579	0.639	13844	0.398								
3.73	0.62	M	514	0.967	7493	0.080	88	0.033	11589	1.124								
3.87	0.43	M	473	0.955	2875	0.178	56	0.045	4389	1.622								
3.97	0.34	M	408	0.501	3336	0.254	343	0.445	5495	0.105	44	0.054	3981	1.526				
4.05	0.24	M+H2	413	0.697	2764	0.372	336	0.220	4955	0.077	61	0.083	3054	2.226				
4.10	0.19	H2	479	0.440	4987	0.093	406	0.441	13923	0.174	35	0.119	4729	1.365				
4.15	0.16**	H2+H3	465	0.454	3690	0.138	406	0.448	5819	0.693	67	0.098	1157	2.923				
4.20	0.13**	H2+H3	546	0.677	6613	0.143	375	0.099	4778	0.624	232	0.096	9826	0.688	33	0.127	3804	1.865
4.25	0.04**	H2+H3	570	0.346	5785	0.241	389	0.400	14424	0.273	49	0.254	2594	1.892				
4.30	0.01**	H3	29	1.000	3843													

* Paramagnetic signal intensity (i.e. excludes intensity from diamagnetic Li signal at ~0 ppm) corrected by accounting for transverse relaxation (T2) effects.

** Nominal Li content based on the measured capacity. Given that parasitic electrochemical reactions tend to occur when cycling LNO above 4.1 V vs. Li/Li^+, this nominal Li content underestimates the true Li content in the bulk cathode above this potential.

ESI Note 4. Composition of the fatigued LNO domains in C4.3V samples from combined ^{7}Li solid-state NMR and synchrotron XRD analysis

^{7}Li solid-state NMR can provide unique insights into the Li content in the fatigued domains in electrochemically cycled LNO samples. As mentioned in the main text, for LNO, the dominant contribution to the observed ^{7}Li shift is the paramagnetic shift, which depends sensitively on the amount of unpaired electron spin density at the Li nucleus, and hence on the number and type of Ni-O-Li bond pathways connecting nearby paramagnetic $Ni^{2+/3+}$ species to the Li nucleus. More specifically, each $Ni^{2+/3+}$ species in the first and second cation coordination shell around Li contributes a certain amount of paramagnetic shift that depends on the extent of Ni *d* - O *p* - Li *s* orbital overlap, hence on the Li–O and Ni–O bond lengths, and on the Li–O–Ni bond angle, as well as on the Ni oxidation state. The total (observed) ^{7}Li shift is then the sum over all Ni-O-Li bond pathway contributions, and as such provides information about the local distribution of Ni oxidation states and on the distribution of Li species within each phase in the *ex situ* LNO sample.

Evolution of the ^{7}Li NMR spectra collected on *ex situ* LNO samples obtained during the first charge process: The ^{7}Li spin echo spectra collected on *ex situ* samples stopped at different stages of the first charge process are shown in **Fig. S9**, and the NMR parameters derived from fits of those spectra are presented in **Table S3**. Spectral evolution of LNO on charge is consistent with prior work.[14] On initial charge, the nominal Li content in LNO can be derived from the capacity since the Li content in the cathode at the start of the charge process is known. The sample labeling scheme adopted hereafter and in **Fig. S9** comprises the symmetry label of the LNO phase(s) present in the sample at a given state of charge and the nominal Li content derived from the specific capacity. For example, the pristine cathode is labeled $H1_{0.98}$ as it is comprised of the initial *R*-3*m* hexagonal phase (H1) and contains 0.98 Li per formula unit. The main resonance in the pristine LNO ($H1_{0.98}$) spectrum appears at ca. 700 ppm, with a minor signal (corresponding to approximately 11% of the Li intensity) at 450 ppm that has been assigned to Li near twin boundaries in our prior work.[12] This secondary signal disappears at an early stage on charge and does not reappear on subsequent discharge due to sluggish Li reintercalation into the strained lattice sites near twin boundaries; it is therefore not considered in our analysis. The 700 ppm resonance corresponds to Li in defect-free, stoichiometric $LiNiO_2$, which interacts with 12 Ni^{3+} species via six 180˚ and six double 90˚ Ni-O-Li interactions.[12]

While one would expect the ^{7}Li shift of the main LNO resonance to decrease during the charge process as Ni^{3+} is oxidized to diamagnetic Ni^{4+}, the chemical shift instead evolves non monotonically (see **Fig. S9**), presumably due to the various structural changes occurring on charge, including phase transformations and changes in the interlayer spacing revealed by synchrotron XRD. The absence of a one-to-one correspondence between ^{7}Li shift and Li content in LNO underscores the need to use synchrotron XRD and NMR results in tandem to identify the nature (structure and composition) of the fatigued domains. The shift of main ^{7}Li resonance first decreases from 700 to 410 ppm as the Li content decreases from 0.98 ($H1_{0.98}$ sample) down to 0.24 ($(M/H2)_{0.24}$ sample). As the Li content in LNO further decreases from 0.24 to 0.04, an increase in the ^{7}Li shift is observed from 410 to 570 ppm despite the average increase in the number of diamagnetic Ni^{4+} neighbors; this increase in the ^{7}Li shift is attributed to the significant decrease in the *a* and *c* lattice parameters as the structure transforms from M to H2, and from H2 to H3.

Determination of the Li content of fatigued domains formed in the C4.3V sample series:

C4.3V-1: As mentioned earlier, for samples collected during the first charge process, the Li content can be computed from the specific capacity, assuming no electrochemical side-reactions. Given that electrolyte decomposition reactions are catalyzed at the surface of LNO particles above 4.1V[15–17] and will also contribute to the specific capacity, the Li content computed from coulometry for C4.3V-1, which comes out

as 0.01, is slightly underestimated. Our prior work[12] has shown that the irreversible capacity (IRC) from surface effects can be deconvolved by taking the difference in IRC between a cell cycled up to 4.3 V (35(2) mAh g^{-1}), with contributions to IRC from both bulk and surface effects, and a cell cycled up to 4.1 V (31(1) mAh g^{-1}), with only contributions to IRC from the bulk. This difference in IRC corresponds to a Li content of approximately 0.02, *which gives an expected Li content of 0.03 for C4.3V-1.*

C4.3V-10: The Rietveld refinement of the synchrotron XRD pattern collected on C4.3V-10 (**Fig. S4b**) indicates a mixture of H2 and H3 phases in the sample, and a fit of the corresponding ^{7}Li NMR spectrum reveals three Li environments at 480 ppm, 410 ppm, and 50 ppm, as shown in **Fig. S10a**. The phase composition and lineshape of the ^{7}Li spectrum obtained for this sample match extremely well those obtained for the $(H2/H3)_{0.16}$ sample on initial charge (see comparison of ^{7}Li spectra in **Fig. S8b**). *From this*, *we deduce that the overall Li content for the C4.3V-10 sample is very close to 0.16.*

C4.3V-50: In the case of the C4.3V-50 sample, its synchrotron XRD pattern can be refined with a single M phase, but the six paramagnetic ^{7}Li signals present in the corresponding NMR spectrum (see fitted spectrum in **Fig. S11a**) suggest the presence of multiple M phases with lattice parameters that are too similar to be resolved in the synchrotron XRD pattern. In fact, a linear combination of the spectra collected on the $M_{0.43}$ and $M_{0.34}$ samples obtained during the first charge process is able to reproduce almost perfectly the lineshape of the C4.3V-50 spectrum, as shown in **Fig. 4**, except from the signals at 700 and 1100 ppm that correspond to electrochemically-inactive domains. From this analysis, the phase fraction based on ^{7}Li NMR signal intensity with T2 correction in the C4.3V-50 spectrum associated with the $H1_{0.98}$, $M_{0.43}$ and $M_{0.34}$ phases comes out as 0.03%, 21%, and 79%, respectively. These phase fractions are then scaled by the respective Li content in each phase to obtain a Li contribution of 0.00029 (0.0003*0.98), 0.09 (0.21*0.43) and 0.27 (0.79*0.34), *which sums to 0.36 for C4.3V-50*.

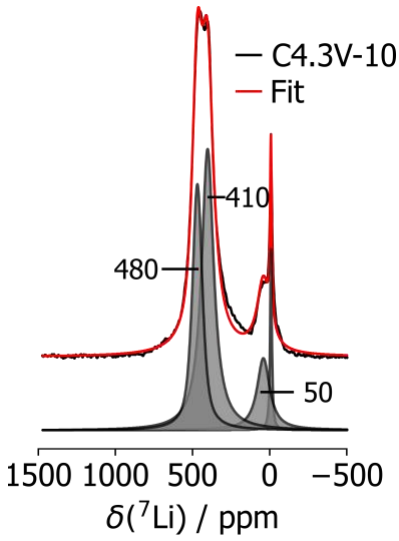

Fig. S10 (a) Fit of the ^{7}Li NMR spectrum obtained on C4.3V-10, revealing three Li resonances at 480 ppm, 410 ppm, and 50 ppm.

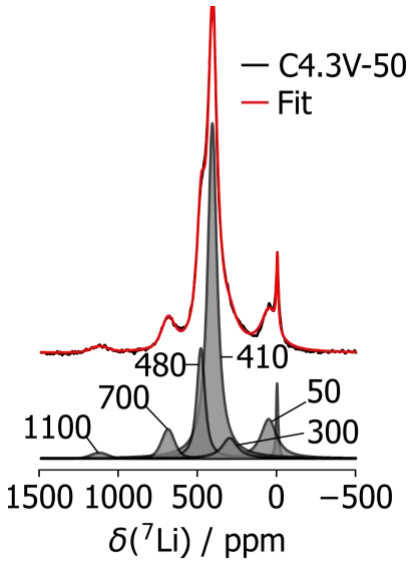

Fig. S11 Fit of the ^{7}Li NMR spectrum obtained on C4.3V-50, revealing six Li resonances at 1100 ppm, 700 ppm, 480 ppm, 410 ppm, 50 ppm, and 0 ppm.

References

1 A. A. Coelho, *J. Appl. Crystallogr.*, 2018, **51**, 210–218.

2 D. Massiot, F. Fayon, M. Capron, I. King, S. Le Calve, B. Alonso, J.-O. Durand, B. Bujoli, Z. Gan and G. Hoatson, *Magn. Reson. Chem.*, 2002, **40**, 70–76.

3 L. de Biasi, A. Schiele, M. Roca-Ayats, G. Garcia, T. Brezesinski, P. Hartmann and J. Janek, *ChemSusChem*, 2019, **12**, 2240–2250.

4 M. Mock, M. Bianchini, F. Fauth, K. Albe and S. Sicolo, *J. Mater. Chem. A*, 2021, **9**, 14928–14940.

5 M. E. Arroyo y de Dompablo, A. Van der Ven and G. Ceder, *Phys. Rev. B - Condens. Matter Mater. Phys.*, 2002, **66**, 1–9.

6 P. W. Stephens, *J. Appl. Crystallogr.*, 1999, **32**, 281–289.

7 M. Juelsholt, J. Chen, M. A. Pérez-osorio, G. J. Rees, S. De Sousa, H. E. Maynard-casely, J. Liu, M. Everett, S. Agrestini, M. Garcia-, K. Zhou, R. A. House and P. G. Bruce, *Chem Rxiv*, , DOI:10.26434/chemrxiv-2023-n6tx4.

8 C. Xu, K. Märker, J. Lee, A. Mahadevegowda, P. J. Reeves, S. J. Day, M. F. Groh, S. P. Emge, C. Ducati, B. Layla Mehdi, C. C. Tang and C. P. Grey, *Nat. Mater.*, 2021, **20**, 84–92.

9 S. Schweidler, L. De Biasi, G. Garcia, A. Mazilkin, P. Hartmann, T. Brezesinski and J. Janek, *ACS Appl. Energy Mater.*, 2019, **2**, 7375–7384.

10 A. Aishova, G. T. Park, C. S. Yoon and Y. K. Sun, *Adv. Energy Mater.*, , DOI:10.1002/aenm.201903179.

11 S. Jamil, C. Li, M. Fasehullah, P. Liu, F. Xiao, H. Wang, S. Bao and M. Xu, *Energy Storage Mater.*, 2022, **45**, 720–729.

12 H. Nguyen, R. Silverstein, A. Zaveri, W. Cui, P. Kurzhals, S. Sicolo, M. Bianchini, K. Seidel and R. J. Clément, *Adv. Funct. Mater.*, 2023, 2306168.

13 P. Kurzhals, F. Riewald, M. Bianchini, H. Sommer, H. A. Gasteiger and J. Janek, *J. Electrochem. Soc.*, 2021, **168**, 110518.

14 H. Li, W. Hua, X. Liu-Théato, Q. Fu, M. Desmau, A. Missyul, M. Knapp, H. Ehrenberg and S. Indris, *Chem. Mater.*, 2021, **33**, 9546–9559.

15 F. Riewald, P. Kurzhals, M. Bianchini, H. Sommer, J. Janek and H. A. Gasteiger, *J. Electrochem. Soc.*, 2022, **169**, 020529.

16 R. Pan, E. Jo, Z. Cui and A. Manthiram, *Adv. Funct. Mater.*, 2022, 2211461.

17 C. S. Yoon, D. W. Jun, S. T. Myung and Y. K. Sun, *ACS Energy Lett.*, 2017, **2**, 1150–1155.